



Contents lists available at ScienceDirect

## International Journal of Solids and Structures

journal homepage: [www.elsevier.com/locate/ijsolstr](http://www.elsevier.com/locate/ijsolstr)

# Tangential continuity of the curvature tensor at grain boundaries underpins disclination density determination from spatially mapped orientation data

C. Fressengeas\*, B. Beausir

Laboratoire d'Etude des Microstructures et de Mécanique des Matériaux LEM3, Université de Lorraine/CNRS/Arts et Métiers ParisTech 7 rue Félix Savart, Metz Cedex 3 57073, France



## ARTICLE INFO

## Article history:

Received 23 May 2018

Revised 6 August 2018

Available online 23 August 2018

## Keywords:

Dislocations

Disclinations

Grain boundaries

Electron backscatter diffraction (EBSD)

## ABSTRACT

Tangential continuity at grain boundaries confers to the curvature tensor smoothness properties needed for the determination of the components of the disclination density tensor available from the orientation maps provided by electron backscattered diffraction measurements. The smoothness implied by attributing a gradient status to the curvature tensor is overachieving and leads to uniformly vanishing disclination density fields. We detail the appropriate field representations for the rotation and curvatures built from the discrete orientation data sets, as well as the relevant numerical differentiation procedures. Illustrations are provided by using both simple constructed data sets and actual measurements.

© 2018 Elsevier Ltd. All rights reserved.

## 1. Introduction

In the theory of crystal defects, discontinuities of elastic rotation fields across bounded surfaces in the material are rendered continuously by smooth non-vanishing disclination density fields (deWit, 1970). Building smooth disclination density fields from discrete orientation maps provided by electron backscattered diffraction (EBSD) measurements, was the objective of earlier work (Beausir and Fressengeas, 2013). This task raises the issues of whether a discrete rotation data set should be regarded as reflecting a continuously differentiable field everywhere or if surfaces of rotation discontinuity exist in the material, and in the latter case, how are the curvature and disclination density tensors fields built at such surfaces? In practice, these issues boil down to how numerical differentiation of the rotation and curvature data sets should be carried out at grain boundaries. Suited algorithms were designed in this aim in Beausir and Fressengeas (2013) and applied to various metallic and geophysical materials, which led to physically consistent interpretations of the structure of grain boundaries in terms of disclination density dipoles at various resolution length scales (Fressengeas et al., 2014; Cordier et al., 2014; Sun et al., 2016). However the minimal differentiability properties required of the rotation and curvature fields to build smooth disclination density fields along surfaces of rotation discontinuity were not detailed and the algorithms used in this work were not available.

In regard to the growing interest in the role of elastic curvatures and disclinations in describing the microstructure of grain boundaries at various length scales (particularly for high-angle boundaries) (Carter et al., 2015; Giacchino and Fonseca, 2015; Rösner et al., 2011; Upadhyay et al., 2016) and their migration under stress (Taupin et al., 2014), we believe that this information should be provided, because it is useful to experimentalists and more generally to those interested in understanding how a smooth disclination density field can account for a bounded rotation discontinuity. In this aim, we give in Section 3 of this paper a primer on the continuous representation of lattice incompatibility in terms of dislocation and disclination density fields, after setting up our notations in Section 2. The field representations of the rotation and curvature data, the required differentiability and the differentiation schemes to be used for the determination of the disclination densities are then described in Section 4. Together with disclination density fields derived from EBSD maps, fields built from simple constructed maps are also shown in this Section for illustration of the basic concepts. Conclusions follow.

## 2. Notations

A bold symbol denotes a tensor, as in:  $\mathbf{A}$ . When there may be ambiguity, an arrow is superposed to represent a vector:  $\vec{\mathbf{A}}$ . The transpose of tensor  $\mathbf{A}$  is  $\mathbf{A}^t$ . The unit second order tensor is denoted  $\mathbf{I}$ . All tensor subscript indices are written with respect to the basis  $(\mathbf{e}_i, i = 1, 2, 3)$  of a rectangular Cartesian coordinate system. Vertical arrays of one or two dots represent contraction of the re-

\* Corresponding author.

E-mail address: [claud.fressengeas@univ-lorraine.fr](mailto:claud.fressengeas@univ-lorraine.fr) (C. Fressengeas).

spective number of "adjacent" indices on two immediately neighboring tensors, in standard fashion. For example, the tensor  $\mathbf{A}\mathbf{B}$  with components  $A_{ik}B_{kj}$  results from the dot product of tensors  $\mathbf{A}$  and  $\mathbf{B}$ , and  $\mathbf{A} : \mathbf{B} = A_{ij}B_{ij}$  represents their inner product. The trace  $A_{ii}$  of tensor  $\mathbf{A}$  is denoted  $\text{tr}(\mathbf{A})$ . The cross product of a second order tensor  $\mathbf{A}$  and a vector  $\mathbf{V}$ , and the **curl** operation for second order tensors is defined row by row, in analogy with the vectorial case. For example:

$$(\mathbf{A} \times \mathbf{V})_{ij} = e_{jkl}A_{ik}V_l \quad (1)$$

$$(\mathbf{curl} \mathbf{A})_{ij} = e_{jkl}A_{il,k}, \quad (2)$$

where  $e_{jkl} = \mathbf{e}_j \cdot (\mathbf{e}_k \times \mathbf{e}_l)$  is a component of the third-order alternating Levi-Civita tensor  $\mathbf{X}$ , equal to 1 if the  $jkl$  permutation is even,  $-1$  if it is odd and 0 otherwise. In the component representation, the comma followed by a component index indicates a spatial derivative with respect to the corresponding Cartesian coordinate as in relation (2). A vector  $\vec{\mathbf{A}}$  is associated with tensor  $\mathbf{A}$  by using the inner product of  $\mathbf{A}$  with tensor  $\mathbf{X}$ :

$$(\vec{\mathbf{A}})_k = -\frac{1}{2}(\mathbf{X} : \mathbf{A})_k = -\frac{1}{2}e_{kij}A_{ij} \quad (3)$$

$$(\mathbf{A})_{ij} = -(\mathbf{X}\vec{\mathbf{A}})_{ij} = -e_{ijk}(\vec{\mathbf{A}})_k. \quad (4)$$

Given a unit vector  $\mathbf{n}$  normal to an interface  $I$  in a domain  $D$  and orienting  $I$  from the sub-domain  $D^-$  to sub-domain  $D^+$ , the normal part  $\mathbf{A}_n$  and tangential part  $\mathbf{A}_t$  of tensor  $\mathbf{A}$  are

$$\mathbf{A}_n = \mathbf{A} \cdot \mathbf{n} \otimes \mathbf{n} \quad (5)$$

$$\mathbf{A}_t = \mathbf{A} - \mathbf{A}_n. \quad (6)$$

For a vector  $\mathbf{V}$ :

$$\mathbf{V}_n = (\mathbf{V} \cdot \mathbf{n})\mathbf{n} = V_n \mathbf{n} \quad (7)$$

$$\mathbf{V}_t = \mathbf{V} - \mathbf{V}_n. \quad (8)$$

The discontinuity of a tensor  $\mathbf{A}$  at the interface  $I$  is denoted  $[[\mathbf{A}]] = \mathbf{A}^+ - \mathbf{A}^-$ , where  $\mathbf{A}^-$  and  $\mathbf{A}^+$  are the values of tensor  $\mathbf{A}$  when evaluated at limit points on the interface along direction  $\mathbf{n}$ , from the left in  $D^-$  and from the right in  $D^+$ , respectively.

### 3. Continuous modeling of lattice incompatibility

In his 1907 paper, Volterra introduced six types of line defects in crystals (Volterra, 1907). Three of them, known as dislocations, are translational defects. The other three, referred to as disclinations, have rotational character. In Volterra's account of dislocations, the displacement field  $\mathbf{u}$  is elastic and has a constant discontinuity  $[[\mathbf{u}]]$  across a surface bounded by the dislocation line, but the (elastic) distortion (strain  $\epsilon$  and rotation  $\omega$ ) field  $\mathbf{U}$  and its derivatives are continuous across this surface, except at the dislocation line where a distortion singularity takes place. A line integral of the distortion field along a closed curve encircling the dislocation line, *i.e.* a Burgers circuit, provides the discontinuity  $[[\mathbf{u}]]$ . This result does not depend on the closing curve and is referred to as the Burgers vector of the dislocation  $\mathbf{b} = [[\mathbf{u}]]$ . Instead of Volterra's representation of dislocations, where the core is seen as a curvilinear hole and the body is multiply connected, we use here a continuous setting, in which the description is regularized by viewing the body as compact and simply connected, and by acknowledging the existence of a narrow but not infinitely thin core region where the displacement field smoothly describes the jump  $\mathbf{b}$ . This choice implies that the resolution length scale is shorter

than in Volterra's description, but a Burgers circuit sufficiently distant from the core still leads to the same Burgers vector  $\mathbf{b}$ . We then consider distortion fields  $\mathbf{U}$ , sufficiently smooth everywhere, which are irrotational outside the core and whose non-vanishing curl defines a smooth dislocation density tensor field  $\alpha$  in the core region. For small distortions,

$$\alpha = \mathbf{curl} \mathbf{U}. \quad (9)$$

In the absence of disclinations, the (elastic) curvature tensor is the gradient of the rotation vector:  $\kappa = \mathbf{grad} \vec{\omega}$ , while the strain tensor  $\epsilon$  retains the smoothness needed to compute its curl. As a result, Eq. (9) reads as well

$$\alpha = \mathbf{curl} \epsilon + \text{tr}(\kappa)\mathbf{I} - \kappa^t. \quad (10)$$

When disclinations are also present, an additional discontinuity  $[[\omega]]$  of the rotation tensor field  $\omega$  (and vector field  $\vec{\omega}$ ) exists over surfaces  $S$  bounded by the disclination lines in the multiply connected body. In practice, the surfaces  $S$  are found almost exclusively along grain or sub-grain boundaries. The strength of a disclination is characterized by its Frank vector  $\Omega = [[\vec{\omega}]]$ , *i.e.* by the discontinuity of the rotation vector over the bounded surfaces  $S$ . Therefore, the rotation is not differentiable across surfaces  $S$  and the curvature  $\kappa$  ceases to be a gradient tensor. However, the strain field  $\epsilon$  retains continuity across  $S$ , except at the dislocation line, and Eq. (10) still holds in this form. By adopting deWit's continuous setting (deWit, 1970), we now acknowledge the finiteness of the core region of the disclination, and view the rotation field as describing smoothly the jump  $\Omega$  across this core. Hence, a Burgers circuit sufficiently distant from the core still yields the Frank vector  $\Omega$ . In deWit's representation, the curvature tensor field  $\kappa$  is a sufficiently smooth field (including across surface  $S$ , in a sense to be described below) reducing to a gradient field (irrotational) outside the core, and whose non-vanishing curl defines the disclination density tensor in the core region:

$$\theta = \mathbf{curl} \kappa. \quad (11)$$

Thus, the defect density tensors  $\theta$  and  $\alpha$  appear as smooth renditions of the Frank and Burgers vectors ( $\Omega$ ,  $\mathbf{b}$ ) respectively. Of course, the smoothness demanded of  $\kappa$  in Eq. (11) does not imply that it be the gradient of the rotation vector, as this would result in  $\theta = 0$  being the only possibility. Actually, tangential continuity of  $\kappa$  is required across surface  $S$  to perform the partial differentiations involved in Eq. (11), but normal discontinuity is allowed, which reads

$$[[\kappa]] \times \mathbf{n} = 0, \quad (12)$$

if  $[[\kappa]]$  denotes the curvature discontinuity across  $S$  and  $\mathbf{n}$  is the normal unit vector to  $S$ . This result was shown in Fressengeas et al. (2012) and a similar result was given earlier in Acharya (2007) in the context of dislocations. We summarize the proof hereafter and adapt it to the present purposes. In Fig. 1, we consider a crystalline domain  $D$  separated into two crystals  $D^-$  and  $D^+$  by the boundary  $S$ . The Burgers circuit  $C$  bridges the boundary and limits the patch  $\Sigma$  over which we now integrate the disclination density tensor:

$$\Omega = \int_{\Sigma} \theta \cdot \mathbf{n} dS = \int_C \kappa \cdot d\mathbf{x}. \quad (13)$$

The result is the Frank vector  $\Omega$  over surface  $\Sigma$ , and the surface integral over  $\Sigma$  may be transformed into a line integral of the curvature along the circuit  $C$  at the r.h.s. of this relation. By letting  $(h^-, h^+)$  and  $L$  tend to zero in Fig. 1, the circuit  $C$  collapses to the point  $P$  on the boundary. As a result, the Frank vector tends to zero on the l.h.s., while the r.h.s. tends to  $[[\kappa]] \cdot \mathbf{I}$ . Hence, we find the relation

$$\forall \mathbf{l} \in S, [[\kappa]] \cdot \mathbf{l} = 0, \quad (14)$$

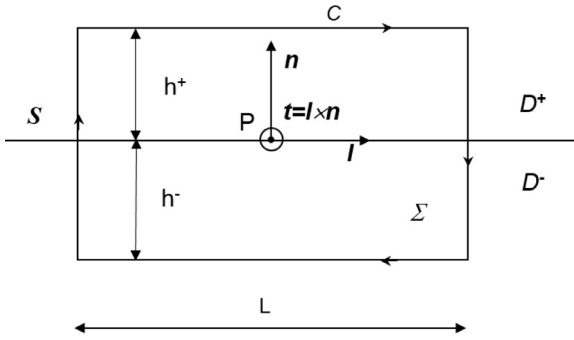


Fig. 1. Burgers circuit  $C$  and patch  $\Sigma$  bounded by  $C$ , across the grain boundary  $S$  separating the crystalline domain  $D$  into two grains  $D^-$  and  $D^+$ .  $\mathbf{n}$ : unit normal vector to the boundary,  $\mathbf{I}$ ,  $\mathbf{t} = \mathbf{I} \times \mathbf{n}$ , orthogonal unit vectors in the boundary.

which is valid for all unit vectors  $\mathbf{I}$  in the boundary  $S$  ( $\mathbf{n} \cdot \mathbf{I} = 0$ ). Thus, Eq. (14) reflects the tangential continuity of the curvature tensor  $\kappa$  along  $S$ , and reads in a more compact form as Eq. (12). Summarizing the proof above, it appears that if Eq. (11) and the representation of (elastic) curvature incompatibility by a smooth disclination density tensor are accepted, then tangential continuity of the curvature tensor across a surface of rotation discontinuity should also be accepted. Normal discontinuity of the curvature tensor is unconstrained by Eq. (14):  $[[\kappa]] \cdot \mathbf{n}$  may well be non-zero. In this case,  $\kappa$  cannot be the gradient of the rotation, and yet the disclination densities can be calculated. As an illustration, consider the wedge disclination density field  $\theta_{33} = \kappa_{32,1} - \kappa_{31,2}$  obtained from the tilt map  $\omega_3$  and curvatures ( $\kappa_{31} = \omega_{3,1}$ ,  $\kappa_{32} = \omega_{3,2}$ ) in the plane ( $\mathbf{e}_1, \mathbf{e}_2$ ) of the reference frame ( $\mathbf{I} = \mathbf{e}_1$ ,  $\mathbf{n} = \mathbf{e}_2$ ,  $\mathbf{t} = \mathbf{I} \times \mathbf{n} = \mathbf{e}_3$ ) shown in Fig. 1. The tangential continuity condition (12) then simply reads:  $[[\kappa_{31}]] = 0$ . Together with this condition, the minimal differentiability requirement needed to compute the partial derivative  $\kappa_{31,2}$  across the boundary in Eq. (11) is the identity of the derivatives  $\kappa_{31,2}^-$  and  $\kappa_{31,2}^+$  from the left and right of the boundary:  $[[\kappa_{31,2}]] = 0$ . The normal jump  $[[\kappa_{32}]]$  is not constrained by Eq. (12) and may not vanish, but the computation of  $\theta_{33}$  only requires differentiation of  $\kappa_{32}$  along the boundary, which demands sufficient smoothness within the grains, not across the boundary.

#### 4. Numerical schemes and examples

As mentioned above, the rotation  $\omega$  is not differentiable across a surface of discontinuity  $S$ . However,  $\omega$  remains backward-differentiable at limit points to the left of  $S$  and forward-differentiable at limit points to its right. Thus, numerical approximations can still be used: we may employ a one-sided finite difference scheme involving backward finite differences to the left of surface  $S$  (of the type  $-(f(x - \Delta x) - f(x))/\Delta x$  at point  $x$ ,  $\Delta x > 0$ ) and forward differences to its right ( $(f(x + \Delta x) - f(x))/\Delta x$  at point  $x$ ,  $\Delta x > 0$ ). In either case, no rotation value from the opposite side of  $S$  is employed. Therefore, such a scheme accounts for the rotation discontinuity and builds the curvature field  $\kappa$  accordingly. In contrast and as detailed above,  $\kappa$  has sufficient smoothness across surface  $S$  to allow forward differentiation both along and across the boundary in the computation of the disclination density tensor  $\theta$  through Eq. (11). As illustrated by the forthcoming examples and results in Beusir and Fressengeas (2013) and Cordier et al. (2014), consistent disclination density fields are found from discrete orientation maps when one-sided numerical differentiation of the rotation data is used for building the curvature field and forward differentiation of the latter for computing the disclination density field. In contrast, uniformly vanishing disclination density fields are obtained when forward differentiation of both rotation and curvature fields is employed, as reported by

Leff et al. (2017) and exemplified in the following. Similarly, vanishing disclination density fields would result from using one-sided differentiation of both fields.

We now showcase these developments by first testing our algorithms in a constructed configuration where the results can be simply and consistently checked. In this aim, we designed the bicrystal shown in Fig. 2a. A tilt boundary is built along the  $\mathbf{e}_1$  direction between the top and bottom grains. The pixel size is assumed to be  $\Delta x_1 = \Delta x_2 = 1 \mu\text{m}$  in both directions ( $\mathbf{e}_1, \mathbf{e}_2$ ), and the tilt angle is  $45^\circ$  around the direction  $\mathbf{e}_3$ . The orientation angle is kept constant throughout the bottom and top grains, except for a sub-grain with a  $\pm 3^\circ$  tilt disorientation across the sub-grain boundaries. The grain and sub-grain boundaries are normal to the unit vectors ( $\mathbf{e}_1, \mathbf{e}_2$ ) and oriented by these vectors. This elementary but revealing configuration allows illustrating the relations between the disclination density field and the disorientation discontinuities along the boundary, as well as highlighting the differences in the algorithm outcomes. The only non-vanishing components of the rotation vector and disclination density tensor accessible from this orientation map are respectively  $\omega_3$  and the wedge-disclination density  $\theta_{33}$  already discussed. As shown above, the tangential continuity condition (12) along the boundary reads  $[[\kappa_{31}]] = 0$ . We note at once from Fig. 2a that, from both forward and one-sided differentiation of the elastic rotation field,  $\kappa_{31} = \omega_{3,1} = 0$  at all pixels in the bottom grain, and  $\kappa_{31} \neq 0$  along two rows in the top grain, as shown in the panel Fig. 2b. If one-sided differentiation is adopted along the grain boundary, then  $\kappa_{32} = \omega_{3,2} = 0$  at all pixels, whereas  $\kappa_{32} \neq 0$  along the boundary if forward differentiation is used, as shown in panel Fig. 2c. Consider calculating the disclination density at all points by using forward differentiation for both rotations and curvatures. For example, at pixel  $A$  surrounded by pixels  $(B, C, D)$ , we find successively:

$$\begin{aligned} \kappa_{32,1}(A) &\cong \frac{1}{\Delta x_1} \left( \frac{\omega_3(D) - \omega_3(B)}{\Delta x_2} - \frac{\omega_3(C) - \omega_3(A)}{\Delta x_2} \right) \\ &= (0.733 - 0.785) \text{ rad} \cdot \mu\text{m}^{-2} \\ \kappa_{31,2}(A) &\cong \frac{1}{\Delta x_2} \left( \frac{\omega_3(D) - \omega_3(C)}{\Delta x_1} - \frac{\omega_3(B) - \omega_3(A)}{\Delta x_1} \right) \\ &= (0.000 - 0.052) \text{ rad} \cdot \mu\text{m}^{-2} \\ \theta_{33}(A) &= \kappa_{32,1}(A) - \kappa_{31,2}(A) = 0. \end{aligned} \quad (15)$$

Such a result is obtained as well at all other pixels and the  $\theta_{33}$  disclination density field is therefore uniformly vanishing, as explained above. Note that we stop differentiating one row before the bicrystal edges to avoid spurious values along these edges. Now consider calculating  $\theta_{33}$  by using one-sided differentiation of the rotation field in building the curvature fields and forward differentiation of the curvature fields in constructing the disclination field. From the above results, we find at pixel  $A$ :

$$\begin{aligned} \kappa_{32,1}(A) &= 0 \\ \kappa_{31,2}(A) &\cong -\frac{\omega_3(B) - \omega_3(A)}{\Delta x_1 \Delta x_2} = -0.052 \text{ rad} \cdot \mu\text{m}^{-2} \\ \theta_{33}(A) &= -\kappa_{31,2}(A) = 0.052 \text{ rad} \cdot \mu\text{m}^{-2}. \end{aligned} \quad (16)$$

When conducted at pixel  $B$ , the calculation leads to  $\theta_{33}(B) = -0.052 \text{ rad} \cdot \mu\text{m}^{-2}$ , and to  $\theta_{33} = 0$  at all other pixels. Note that the disclination density values are affected at the pixel centers and that the values between pixels may be obtained by using interpolation procedures: As a consequence, the disclination density value at a boundary point, for example between pixels  $A$  and  $C$ , is common to both grains and is a property of the interface. The positive  $\theta_{33}(A)$  and negative  $\theta_{33}(B)$  spots form a wedge disclination dipole terminating the bounded surface  $AB$  along the grain boundary, across which a discontinuity  $[[\omega_3]] = -3^\circ$  of the rotation takes place. The Frank vectors of the disclinations are there-

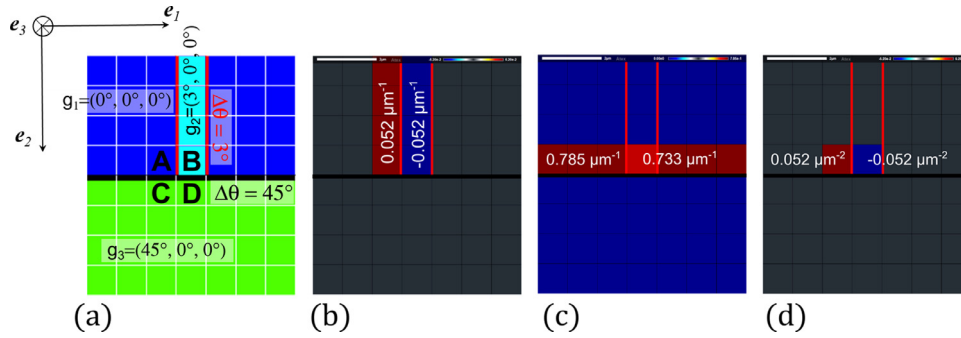


**Fig. 2.** Constructed bicrystal with 45° tilt boundary. (a) Configuration. Euler angles: bottom (green) grain (45°, 0°, 0°), top (dark blue) grain (0°, 0°, 0°), (pale blue) sub-grain inserted in top grain (3°, 0°, 0°). The first Euler angle (precession) is measured around unit vector  $e_3$  in the orthonormal sample frame ( $e_1, e_2, e_3$ ). The pixel size is 1  $\mu\text{m}$ ; (b) Curvature field  $\kappa_{31}$  derived from one-sided differentiation of the elastic rotation field  $\omega_3$ ; (c) Curvature field  $\kappa_{32}$  derived from forward differentiation of the elastic rotation field  $\omega_3$ ; (d) Wedge disclination density  $\theta_{33}$  derived from forward differentiation of the curvature fields ( $\kappa_{31}, \kappa_{32}$ ). In panels (b,c,d) numbers indicate the non-zero variable values at the appropriate pixels. (For interpretation of the references to colour in this figure legend, the reader is referred to the web version of this article.)

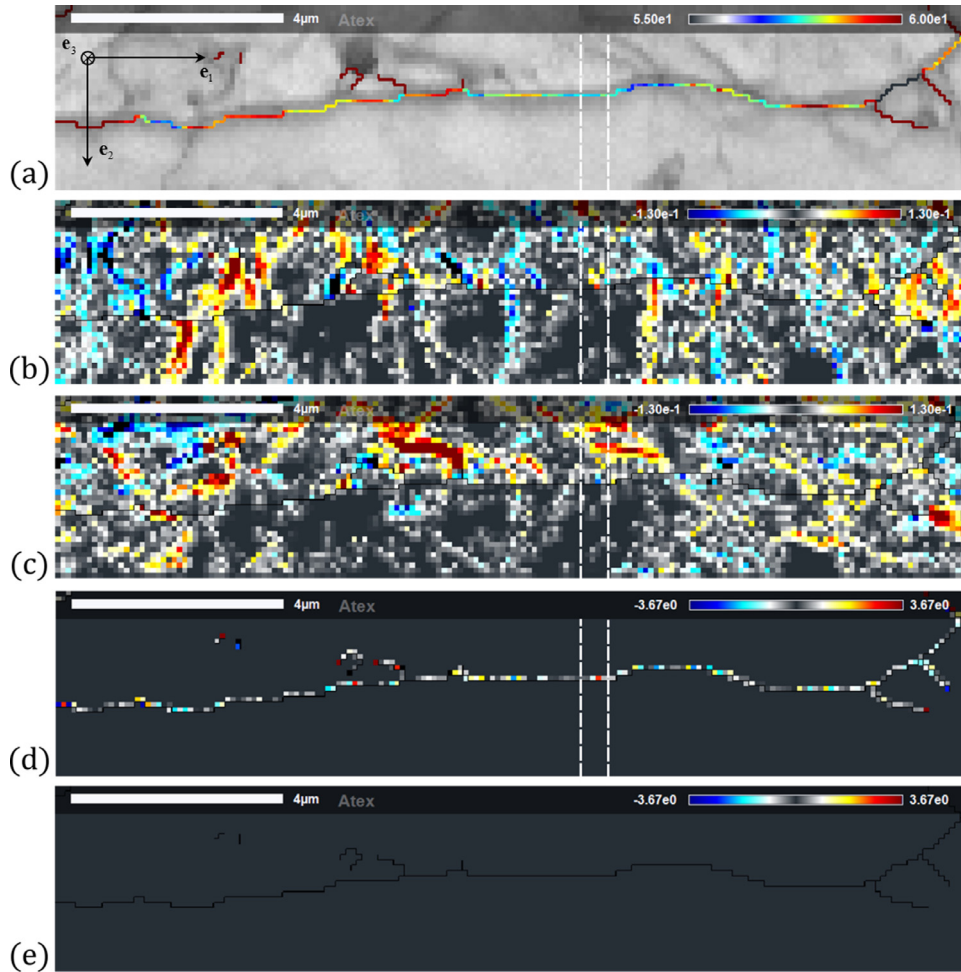


**Fig. 3.** EBSD data in a rolled 99% commercially pure Al reduced by 50%. Reference frame,  $e_1$ : rolling direction,  $e_2$ : normal direction,  $e_3$ : transverse direction. Dimensions of the maps: (17.3  $\mu\text{m} \times 3.5 \mu\text{m}$ ). The vertical dashed lines underline correlations between corresponding features in panels (a) through (d). (a): Grain-to-grain disorientation along a high angle grain boundary (55° through 60°). (b)  $\kappa_{31}$  curvature field obtained from one-sided differentiation of the elastic rotation field  $\omega_3$ ; (c)  $\kappa_{32}$  curvature field obtained from one-sided differentiation of the elastic rotation field  $\omega_3$ ; (d)  $\theta_{33}$  wedge disclination density field obtained from forward differentiation of the curvature fields; (e)  $\theta_{33}$  wedge disclination density field obtained from one-sided differentiation of the curvature fields. Angles provided in degrees, curvatures and disclination densities in  $\text{rad} \cdot \mu\text{m}^{-1}$  and  $\text{rad} \cdot \mu\text{m}^{-2}$  units respectively.

fore  $\Omega = \Omega_3 e_3$  with  $\Omega_3 = [[\omega_3]] = \pm 3^\circ$ . These results are consistent with the definition and properties of disclination dipoles. Cutting the bicrystal along the boundary from B to the right edge to relax the incompatible strains associated with the negative disclination in B would lead to a 3° angular sector overlap of the top and bottom crystals. Further cutting the bicrystal between A and B to

relax the incompatible strains associated with the positive disclination in A would additionally lead to a 3° angular sector gap between the two crystals, so that welding back these crystals would only require a 3° rotation of the segment AB.

We now discuss the determination of disclination density fields from an orientation map obtained from actual EBSD measure-

ments. Although the data set is more complex and extensive, the algorithms are the same as in the above example. The measurements were carried out on a rolled 99.9% commercially pure aluminum sample (50% rolling ratio in one pass), using a Zeiss ULTRA 55 scanning electron microscope. The plane of the maps in Fig. 3 is normal to the transverse direction in rolling and the pixel size is 100 nm. All components  $\omega_i$ ,  $\forall i \in (1, 2, 3)$  of the rotation vector are available from the orientation map, and the panel Fig. 3a shows the grain-to-grain disorientation along a grain boundary. The accessible disclination density components are  $\theta_{i3} = \kappa_{i2,1} - \kappa_{i1,2}$ ,  $\forall i \in (1, 2, 3)$ , where  $\kappa_{i1} = \omega_{i,1}$ ,  $\kappa_{i2} = \omega_{i,2}$  but here, we again focus on the wedge disclination density  $\theta_{33}$  for the sake of conciseness. The  $(\kappa_{31}, \kappa_{32})$  curvature fields obtained from one-sided differentiation of the rotation component  $\omega_3$  are shown in panels Fig. 3(b,c). If one-sided differentiation of these curvature fields is also employed for constructing the disclination density field  $\theta_{33}$ , then  $\theta_{33} = 0$  is found uniformly at all points, as shown in panel Fig. 3e and as already discussed above. In contrast, the values of  $(\kappa_{32,1}, \kappa_{31,2})$  are different when forward differentiation is used, and the disclination density  $\theta_{33}$  is non-vanishing along the boundary, as panel Fig. 3d shows. A configuration similar to the simple example discussed in Fig. 2 can be spotted between the vertical dashed lines. Indeed, although its normal is not known, the grain boundary lies along the horizontal direction  $\mathbf{e}_1$  in this area, the  $\kappa_{32}$  field is approximately constant in both grains and the  $\kappa_{31,2}$  field has a negative value when using forward differentiation across the boundary. Hence, a disclination density dipole is found in panel Fig. 3d. Consistently, a disorientation discontinuity of the order of  $2^\circ$  is seen in panel Fig. 3a. A disorientation discontinuity along the boundary is indeed a beacon of the difference between the mixed second-order partial derivatives of the elastic rotation and of the presence of a disclination at this point, as already illustrated in Fig. 2. Significant  $\theta_{33}$  disclinations may further be noticed in panel Fig. 3d at the ends of sub-grain boundaries, where they clearly correlate with discontinuities in the disorientation. The analysis also provides comprehensive details on how the disorientation discontinuities relate to the variations of the lattice curvatures in their neighborhood, on both sides of the interface. Clearly, such correlations could not be observed if the disclination density distribution were arising from random numerical noise.

## 5. Conclusions

In this paper, we present the fundamental physical background and complementary algorithmic information to the numerical methods introduced in Beausir and Fressengeas (2013) and used in Cordier et al. (2014) to determine smooth disclination density fields from the discrete rotation data sets provided by EBSD measurements. From a general standpoint, thinking of discrete orientation maps as sets of point values picked out from continuously differentiable orientation fields or from fields encountering surfaces of discontinuity is equally valid. However, to ensure consistency of the present methods with classical understanding in the field theory of crystal defects (deWit, 1970), strong variations in the rotation point values across bounded surfaces are viewed in this paper as manifestations of discontinuities of the rotation field. Overly regularization resulting from the interpretation of such data as point values picked out from a continuous rotation field, as in the algorithmic prescriptions of Leff et al. (2017), destroys the account of curvature incompatibility. Therefore, a one-sided finite difference scheme of the rotation along the surfaces of discontinuity is key to the adequate derivation of the curvature field. Consistency of the algorithm with the classical point of view of the field theory of crystal defects then implies that the tangential part of the curvature tensor be seen as continuous along the grain boundaries in building the disclination density fields, whereas the normal part

of the curvature tensor is left unconstrained and may be discontinuous (Fressengeas et al., 2012). This interpretation of the data underpins using a forward finite difference scheme in the computation of the curvature partial derivatives involved in the disclination densities, including the derivatives across the surfaces of rotation discontinuity. It is worth noting that the present algorithmic prescriptions are not specific to the determination of disclination densities from discrete rotation maps. The analogies between Eqs. (9) and (11) suggest indeed that the above arguments would similarly apply to displacements, distortions and dislocations if the latter were to be determined from discrete displacement maps, as obtained for example from Digital Image Correlation methods (Chu et al., 1985; Sutton et al., 1986). In short and duplicating the above arguments, the displacement field would need to be seen as discontinuous across some bounded surface  $S$  and one-sided differentiation would be applied to build the (elastic) distortion field  $\mathbf{U}$  along  $S$ . Then, because tangential continuity of  $\mathbf{U}$  holds across surface  $S$  (Acharya, 2007):

$$[[\mathbf{U}]] \times \mathbf{n} = 0, \quad (17)$$

forward differentiation of  $\mathbf{U}$  could be performed across  $S$ , which would allow evaluating the dislocation density tensor  $\boldsymbol{\alpha}$  through Eq. (9). However, when strain incompatibility is neglected, Eqs. (9) and (10) reduce to  $\boldsymbol{\alpha} \cong \text{tr}(\boldsymbol{\kappa})\mathbf{I} - \boldsymbol{\kappa}^t$ . As a result, this approximation of  $\boldsymbol{\alpha}$  simply stems from the elastic curvatures, and can be directly determined from an orientation map (El-Dasher et al., 2003; Field et al., 2005; Pantleon, 2008; Montagnat et al., 2015). In the absence of disclinations, the curvature tensor  $\boldsymbol{\kappa}$  can be seen as the gradient of the rotation vector and be computed through forward differentiation of the rotation field. In the presence of disclinations,  $\boldsymbol{\kappa}$  is no more a gradient tensor and must be calculated from one-sided differentiation of the rotation field, as detailed above.

## References

- Acharya, A., 2007. Jump condition for GND evolution as a constraint on slip transmission at grain boundaries. *Philos. Mag.* 87, 1349–1359.
- Beausir, B., Fressengeas, C., 2013. Disclination densities from EBSD orientation mapping. *Int. J. Solids Struct.* 50, 137–146.
- Carter, J.L.W., Sosa, J.M., Shade, P.A., Fraser, H.L., Uchic, M.D., Mills, M.J., 2015. The potential link between high angle grain boundary morphology and grain boundary deformation in a nickel-based superalloy. *Mater. Sci. Eng. A* 640, 280–286.
- Chu, T.C., Ranson, W.F., Sutton, M.A., Peters, W.H., 1985. Applications of digital-image-correlation techniques to experimental mechanics. *Exp. Mech.* 25, 232–244.
- Cordier, P., Demouchy, S., Beausir, B., Taupin, V., Barou, F., Fressengeas, C., 2014. Disclinations provide the missing mechanism for deforming olivine-rich rocks in the mantle. *Nature* 507, 51–56.
- deWit, R., 1970. Linear theory of static disclinations. In: Simmons, J.A., deWit, R., Bullough, R. (Eds.), *Fundamental Aspects of Dislocation Theory*. In: *Nat. Bur. Stand. (US), Spec. Publ.*, Vol. 317, Vol. 1, pp. 651–680.
- El-Dasher, B.S., Adams, B.L., Rollett, A.D., 2003. Viewpoint: experimental recovery of geometrically necessary dislocation density in polycrystals. *Scr. Mater.* 48, 141–145.
- Field, D.P., Trivedi, P.B., Wright, S.J., Kumar, M., 2005. Analysis of local orientation gradients in deformed single crystals. *Ultramicroscopy* 103, 33–39.
- Fressengeas, C., Taupin, V., Capolungo, L., 2014. Continuous modeling of the structure of symmetric tilt boundaries. *Int. J. Solids Struct.* 51, 1434–1441.
- Fressengeas, C., Taupin, V., Upadhyay, M., Capolungo, L., 2012. Tangential continuity of elastic/plastic curvature and strain at interfaces. *Int. J. Solids Struct.* 49, 2660–2667.
- Giachino, F.D., Fonseca, J.Q.d., 2015. An experimental study of the polycrystalline plasticity of austenitic stainless steel. *Int. J. Plast.* 74, 92–109.
- Leff, A.C., Weinberger, C.R., Taheri, M.L., 2017. On the accessibility of the disclination tensor from spatially mapped orientation data. *Acta Mater.* 138, 161–173.
- Montagnat, M., Chauve, T., Barou, F., Tommasi, A., Beausir, B., Fressengeas, C., 2015. Analysis of dynamic recrystallization of ice from EBSD orientation mapping. *Front. Earth Sci.* 3, 81. doi:10.3389/feart.2015.00081.
- Pantleon, W., 2008. Resolving the geometrically necessary dislocation content by conventional electron backscattering diffraction. *Scr. Mater.* 58, 994–997.
- Rösner, H., Kübel, C., Ivanisenko, Y., Kurmanaeva, L., Divinski, S.V., Peterlechner, M., Wilde, G., 2011. Strain mapping of a triple junction in nanocrystalline Pd. *Acta Mater.* 59, 7380–7387.
- Sun, X.Y., Taupin, V., Fressengeas, C., Cordier, P., 2016. Continuous description of the atomic structure of grain boundaries using dislocation and generalized-disclination density fields. *Int. J. Plast.* 77, 75–89.

- Sutton, M.A., Cheng, M.Q., Peters, W.H., Chao, Y.J., McNeill, S.R., 1986. Application of an optimized digital image correlation method to planar deformation analysis. *Image Vision Comput.* 4, 143–150.
- Taupin, V., Capolungo, L., Fressengeas, C., 2014. Disclination mediated plasticity in shear-coupled boundary migration. *Int. J. Plast.* 53, 179–192.
- Upadhyay, M.V., Capolungo, L., Taupin, V., Fressengeas, C., Lebensohn, R., 2016. A higher order elasto-viscoplastic model using fast Fourier transforms: effects of lattice curvatures on mechanical response of nanocrystalline metals. *Int. J. Plast.* 83, 126–152.
- Volterra, V., 1907. Sur l'équilibre des corps élastiques multiplement connexes. *Ann. Sci. Ecol. Norm.* 24 (Sup. III), 401–517.